



Diffuse reflection boundary condition for high-order lattice Boltzmann models with streaming–collision mechanism



Jianping Meng, Yonghao Zhang*

James Weir Fluids Laboratory, Department of Mechanical & Aerospace Engineering, University of Strathclyde, Glasgow G1 1XJ, UK

ARTICLE INFO

Article history:

Received 6 May 2013

Received in revised form 6 October 2013

Accepted 30 October 2013

Available online 8 November 2013

Keywords:

Lattice Boltzmann method

High-order model

Diffuse reflection boundary condition

Streaming–collision scheme

ABSTRACT

For lattice Boltzmann (LB) models, their particle feature is ensured by the streaming–collision mechanism. However, this mechanism is often discarded for high-order LB models due to multi-speed lattices. Here, we propose a new way of implementing the diffuse reflection boundary condition that can maintain the characteristic streaming–collision mechanism for high-order models. It is then tested on four lattice models, namely D2Q16, D2Q17, D2Q37 and D3Q121 for isothermal and thermal Couette flows and lid-driven cavity flows. Our implementation is shown to be able to achieve second-order accuracy globally.

© 2013 Elsevier Inc. All rights reserved.

1. Introduction

High-order models have recently attracted considerable interests in the lattice Boltzmann (LB) community. For these models, multi-speed lattices are used while high-order terms in the expanded equilibrium distribution function are retained. By doing so, we can have a few benefits, e.g. consistent description of thermal flows, the Galilean invariance of the transport coefficients, improved model capability for compressible flows and flows beyond the Navier–Stokes hydrodynamics [1–5]. Therefore, high-order models can be applicable to a broad range of flows while the simplicity of the standard LB models can still be preserved. For example, they have been used in simulating complex flow problems including multicomponent and multiphase flows, e.g. Refs. [6–9].

A key feature of high order LB models is that they may be able to capture rarefaction effects beyond the Navier–Stokes level [2,3,10–15] (also see references therein). It was shown that LB models are closely related to kinetic equations due to their kinetic nature as shown by Shan et al. [3]. By reserving more and more high-order terms and employing sufficiently accurate multi-speed lattices, they effectively approach the original kinetic equations [10,11]. For isothermal problems, similarity with the linearized BGK equation has been observed for high-order LB models retaining up to second order terms in the equilibrium distribution [10]. To achieve sufficient accuracy, it is proven to be of importance to choose an appropriate multi-speed lattice [10]. By using modest lattice points, non-continuum effects may be captured for up to the early transition regime [2]. For example, the velocity slip can be captured by a D2Q16¹ model for the Knudsen number up to 0.5. Further analysis has shown that lattices from even order Gauss–Hermite quadrature tend to give more accurate predictions [11]. Thermal flows have also been investigated by using a recently developed high-order LB model which is featured with an adjustable Prandtl number [2]. Some typical non-continuum phenomena (e.g. the stream-wise heat flux for the

* Corresponding author.

E-mail addresses: jianping.meng@strath.ac.uk (J. Meng), yonghao.zhang@strath.ac.uk (Y. Zhang).

¹ Here DmQn refers to the standard terminology, i.e. m dimensions and n lattice points.

thermal Couette flow), which the Navier–Stokes model completely fails to describe, can be captured using modest lattice points while the accuracy is comparable with the so-called R13 model [16].

Implementation of boundary conditions is crucial to application of high-order LB models. Among various candidates, the diffuse reflection boundary condition is of particular interest. This is not only because of its ability to predict velocity slip and temperature jump at the solid boundaries but also because of its feature of maintaining the positivity of distribution function which is the key to numerical stability. Although its implementation has been discussed in Ref. [24], the resulting formula cannot be directly applied for high-order models due to multi-speed lattices. Currently, there is still lack of insightful discussions on how to deal with multi-layer lattices at wall boundary. The successful implementations for the high-order models are based on various finite difference schemes [13,17], where the highly desirable “streaming and collision” mechanism has to be discarded. However, it is worth noting that the “streaming and collision” mechanism is a key ingredient of the LB model. It is this mechanism that makes the LB model a particle-like method: simple numerical scheme and straightforward to implement molecular interactions. From the numerical point view, this simple scheme has second-order accuracy both in space and time due to its Lagrangian nature [25]. As an explicit scheme, the parallelization is easy in comparison with implicit schemes. Therefore, it is of great importance to retain the “streaming and collision” mechanism.

The purpose of this work is to formulate the diffuse reflection boundary condition that can retain the “streaming and collision” feature. The derived implementation will be tested for both isothermal and thermal Couette flows, and lid-driven cavity flow. Here, we would like to emphasize that our aim is to achieve a new way of implementing the diffuse reflection boundary condition so the streaming-collision feature can be kept. The discussion on accuracy of high-order models themselves can be referred to [2,3,10–15].

2. High order lattice Boltzmann models

One systematic procedure to derive high-order LB models is discretizing the Boltzmann–BGK equation (see Refs. [3,18,19] for the details), so that the LB governing equation can be written as

$$\frac{\partial f_\alpha}{\partial t} + c_{\alpha,i} \frac{\partial f_\alpha}{\partial x_i} = -\frac{1}{\tau} (f_\alpha - f_\alpha^{eq}), \quad (1)$$

where f denotes the single-particle distribution function evaluated at a discrete velocity \mathbf{c}_α , f^{eq} is the truncated Maxwellian distribution, while τ is the mean relaxation time. For convenience, a non-dimensional system

$$\begin{aligned} x_k &= \frac{\hat{x}_k}{L}, & u_k &= \frac{\hat{u}_k}{\sqrt{RT_0}}, & t &= \frac{\sqrt{RT_0} \hat{t}}{L}, & c_k &= \frac{\hat{c}_k}{\sqrt{RT_0}}, & T &= \frac{\hat{T}}{T_0}, & \tau &= \frac{\sqrt{RT_0} \hat{\tau}}{L}, \\ f &= \frac{\hat{f}(RT_0)^{D/2}}{\rho_0}, & \rho &= \frac{\hat{\rho}}{\rho_0}, & p &= \frac{\hat{p}}{p_0}, & \mu &= \frac{\hat{\mu}}{\mu_0}, & q_i &= \frac{\hat{q}_i}{p_0 \sqrt{RT_0}}, & \sigma_{ij} &= \frac{\sigma_{ij}}{p_0} \end{aligned}$$

can be introduced in Eq. (1), where the symbols with hat represent the dimensional quantities. The common notations are used to represent physical quantities, i.e. ρ denotes density; μ , dynamic viscosity; u , velocity; p , pressure; T , temperature; σ , stress and q , heat flux. L is the characteristic length of the system. The symbols with subscript 0 are the corresponding reference quantities.

With this non-dimensional system, the equation of state becomes $p = \rho T$. The mean relaxation time can be written explicitly as $\tau = \mu_0 \sqrt{RT_0} \mu / (p_0 L p)$, which is related to viscosity and pressure. Meanwhile, the macroscopic quantities can be obtained as

$$\begin{bmatrix} \rho \\ \rho u_i \\ \sigma_{ij} \\ q_i \\ \rho DT \end{bmatrix} = \sum_{\alpha=1}^d f_\alpha \begin{bmatrix} 1 \\ c_{\alpha,i} \\ C_{\langle \alpha,i} C_{\alpha,j \rangle} \\ \frac{1}{2} C_{\alpha,i} C_{\alpha,i} C_{\alpha,j} \\ C_{\alpha,i} C_{\alpha,i} \end{bmatrix}, \quad (2)$$

where D is the number of space dimensions, d is the number of total discrete velocities, $\mathbf{C}_\alpha = \mathbf{c}_\alpha - \mathbf{u}$ is the peculiar velocity and the angle brackets $\langle \dots \rangle$ indicate the trace-free part of the tensor. The discrete velocity \mathbf{c}_α and its weights w_α may be determined in several ways. For example, Refs. [3,20,21] list explicitly various orders of discrete velocity sets. For convenience, we use the notation $\xi = \{\mathbf{c}_\alpha, w_\alpha\}$, $\alpha = 1 \dots d$ to represent the discrete velocity sets. With an appropriate ξ , the explicit form of the truncated Maxwellian distribution can be given as [3]

$$\begin{aligned} f_\alpha^{eq} &= \rho g_\alpha^{eq} = w_\alpha \rho \left\{ 1 + c_{\alpha,i} u_i + \frac{1}{2} [(c_{\alpha,i} u_i)^2 - u_i u_i + (T - 1)(c_{\alpha,i} c_{\alpha,i} - D)] \right. \\ &\quad + \frac{c_{\alpha,i} u_i}{6} [(c_{\alpha,i} u_i)^2 - 3 u_i u_i + 3(T - 1)(c_{\alpha,i} c_{\alpha,i} - D - 2)] \\ &\quad \left. + \frac{1}{24} [(c_{\alpha,i} u_i)^4 - 6(u_i c_{\alpha,i})^2 u_j u_j + 3(u_j u_j)^2] \right\} \end{aligned}$$

$$\begin{aligned}
& + \frac{T-1}{4} [(c_{\alpha,i} c_{\alpha,i} - D - 2)((u_i c_{\alpha,i})^2 - u_i u_i) - 2(u_i c_{\alpha,i})^2] \\
& + \frac{(T-1)^2}{8} [(c_{\alpha,i} c_{\alpha,i})^2 - 2(D+2)c_{\alpha,i} c_{\alpha,i} + D(D+2)] \Big\}. \quad (3)
\end{aligned}$$

For thermal problems, the fourth-order expansion is needed [3,4]. If an isothermal flow is concerned, the temperature T can be set to be 1. Moreover, to simulate incompressible flows, it is common to use only up to second order terms of f_{α}^{eq} as to be done in the following simulations for isothermal flows.

With Eq. (1) and Eq. (3), the final issue is to choose an appropriate numerical scheme. Following the spirit of “streaming and collision” mechanism [22], an implicit scheme

$$\begin{aligned}
f_{\alpha}(\mathbf{x} + \mathbf{c}_{\alpha} dt, t + dt) - f_{\alpha}(\mathbf{x}, t) &= \frac{dt}{2\tau(\mathbf{x}, t)} [f_{\alpha}^{eq}(\mathbf{x}, t) - f_{\alpha}(\mathbf{x}, t)] + \frac{dt}{2\tau(\mathbf{x} + \mathbf{c}_{\alpha} dt, t + dt)} \\
&\times [f_{\alpha}^{eq}(\mathbf{x} + \mathbf{c}_{\alpha} dt, t + dt) - f_{\alpha}(\mathbf{x} + \mathbf{c}_{\alpha} dt, t + dt)],
\end{aligned}$$

can be constructed. If we introduce a new variable

$$\tilde{f}_{\alpha} = f_{\alpha} + \frac{dt}{2\tau}(f_{\alpha} - f_{\alpha}^{eq}) \quad (4)$$

to eliminate the implicitness, we will get the evolution equation for \tilde{f} as

$$\tilde{f}_{\alpha}(\mathbf{x} + \mathbf{c}_{\alpha} dt, t + dt) - \tilde{f}_{\alpha}(\mathbf{x}, t) = -\frac{dt}{\tau(\mathbf{x}, t) + 0.5 dt} [\tilde{f}_{\alpha}(\mathbf{x}, t) - f_{\alpha}^{eq}(\mathbf{x}, t)]. \quad (5)$$

The advantage of Eq. (5) is that, if the discrete velocities are tied to discretization of the space and time by choosing ξ with integer value, the evolution of \tilde{f}_{α} can be accomplished in a way similar to a “particle”, which makes the LB method simple but still flexible.

With the variable \tilde{f}_{α} , the conservative quantities like density can still be obtained by using Eq. (2) without changing form but some conversions are needed for shear stress and heat flux (cf. Ref. [22]). In addition, the mean relaxation time τ may be related to the local fluid temperature for thermal problems.

3. Diffuse-reflection-type boundary condition

The essential idea of the diffuse-reflection boundary condition is that an outgoing particle completely forgets its history and its velocity is re-normalized by the Maxwellian distribution. To implement this diffuse-reflection principle for a high-order LB model, we will follow the procedure described in Refs. [23,24,26]. Moreover, the discussion is based on the assumption that the effective particle-wall interaction time is small compared to any characteristic time of interest and no permanent adsorption occurs [23].

For the high-order models, as “particles” from more than one layer of computational grids can hit the wall at the same time step, we have to properly identify them in order to implement the boundary condition. For this purpose, N layers of the ghost grids are introduced (see the example of the D2Q17 lattice and its grid arrangement shown in Figs. 1 and 2), where N can be determined via the corresponding maximum value of the discrete velocity heading towards the wall (e.g., $N = 3$ for the D2Q17 lattice). As a common practice, the physical wall is located at the half grid space between the ghost and fluid grids. To further distinguish incoming and outgoing particles, we use $\mathbf{c}'_{\alpha,l}$ and $\mathbf{c}_{\alpha,l}$ to represent their velocities respectively, where l denotes the layer number of the ghost grid ranging from 0 to $N - 1$. Similarly, the distributions of incoming and outgoing particles at the layer l are written as $f_{\alpha,l}^I(\mathbf{x}_w, t)$ and $f_{\alpha,l}^O(\mathbf{x}_w, t)$, where the superscripts I and O stand for ‘incoming’ and ‘outgoing’. The corresponding discrete velocities must satisfy the condition $(\mathbf{c}'_{\alpha,l} - \mathbf{u}_w) \cdot \mathbf{n} dt < -l dx$ and $(\mathbf{c}_{\alpha,l} - \mathbf{u}_w) \cdot \mathbf{n} dt > l dx$, where \mathbf{n} denotes the unit vector normal to the wall surface $\partial\Omega$ at the position \mathbf{x} and directed from the wall into the fluid. Note, in the present lattice system $dx/dt = 1$ so the conditions are equivalent to $(\mathbf{c}'_{\alpha,l} - \mathbf{u}_w) \cdot \mathbf{n} < -l$ and $(\mathbf{c}_{\alpha,l} - \mathbf{u}_w) \cdot \mathbf{n} > l$. Indeed, $\mathbf{c}'_{\alpha,l}$ and $\mathbf{c}_{\alpha,l}$ are a symmetric pair. On the other hand, the known information of the wall, i.e., the position, velocity and temperature, are represented by \mathbf{x}_w , \mathbf{u}_w and T_w .

Firstly, the distribution $f_{\alpha,l}^I(\mathbf{x}_w, t)$ can be obtained by naturally streaming the distribution function at the fluid grids into the corresponding ghost ones. We need to determine the unknown distribution $f_{\alpha,l}^O(\mathbf{x}_w, t)$ according to the principle of diffusion reflection. Similar to the derivation of the continuum version of diffuse-reflection condition [23], we first write down the mass of outgoing and incoming particles as,

$$\mathcal{M}_{\alpha,l}^O = f_{\alpha,l}^O(\mathbf{x}_w, t) dV, \quad \mathbf{x} \in \partial\Omega, (\mathbf{c}_{\alpha,l} - \mathbf{u}_w) \cdot \mathbf{n} > l, \quad (6)$$

$$\mathcal{M}_{\alpha,l}^I = f_{\alpha,l}^I(\mathbf{x}_w, t) dV, \quad \mathbf{x} \in \partial\Omega, (\mathbf{c}'_{\alpha,l} - \mathbf{u}_w) \cdot \mathbf{n} < -l, \quad (7)$$

where \mathcal{M} stands for mass and dV denotes the volume of the grid cell. It is worth noting here that, due to the discretization mechanism and the exact advection of the LB method (cf. Eq. (5)), the flux term in the continuum version (cf. Eq. (1.11.1) in [23]), can be replaced by the distribution function itself. Hence, according to the mass conservation, we have,

$$\mathcal{M}_{\alpha,l}^0 = \sum_l^{N-1} \sum_{(\mathbf{c}'_{\alpha,l} - \mathbf{u}_w) \cdot \mathbf{n} < -l} R(\mathbf{c}'_{\alpha,l} \rightarrow \mathbf{c}_{\alpha,l}, \mathbf{x}_w, t) \mathcal{M}_{\alpha,l}^l, \quad (8)$$

where $R(\mathbf{c}'_{\alpha,l} \rightarrow \mathbf{c}_{\alpha,l}, \mathbf{x}_w, t)$ is the so-called scattering probability. Here it is assumed that various layers of ghost nodes admit the same scattering probability. This is natural as they belong to the same physical wall point. Immediately, we arrive at

$$f_{\alpha,l}^0 = \sum_{l=0}^{N-1} \sum_{(\mathbf{c}'_{\alpha,l} - \mathbf{u}_w) \cdot \mathbf{n} < -l} R(\mathbf{c}'_{\alpha,l} \rightarrow \mathbf{c}_{\alpha,l}, \mathbf{x}_w, t) f_{\alpha,l}^l(\mathbf{x}_w, t). \quad (9)$$

Moreover, the scattering probability R must satisfy the property of non-negativeness, normalization and reciprocity conditions [23]. Particularly, the normalization condition, corresponding to mass conservation under the assumption of no permanent adsorption, can be written as,

$$\sum_{l=0}^{N-1} \sum_{(\mathbf{c}_{\alpha,l} - \mathbf{u}_w) \cdot \mathbf{n} > l} R(\mathbf{c}'_{\alpha,l} \rightarrow \mathbf{c}_{\alpha,l}, \mathbf{x}_w, t) = 1. \quad (10)$$

So far, the discussion is still rather generic as we have not introduced any specific assumption for the diffuse-reflection principle. Therefore, the above formulation may also be used to derive other types of boundary condition.

If the assumption of the diffuse-reflection boundary condition is applied, the scattering probability can be calculated as

$$R_{\mathcal{D}}(\mathbf{c}'_{\alpha,l} \rightarrow \mathbf{c}_{\alpha,l}) = \frac{g_{\alpha}^{eq}(\mathbf{u}_w, T_w)}{\sum_{l=0}^{N-1} \sum_{(\mathbf{c}_{\alpha,l} - \mathbf{u}_w) \cdot \mathbf{n} > l} g_{\alpha}^{eq}(\mathbf{u}_w, T_w)}. \quad (11)$$

Hence, the distributions of outgoing particles can be written as

$$f_{\alpha,l}^0 = \frac{\sum_{l=0}^{N-1} \sum_{(\mathbf{c}'_{\alpha,l} - \mathbf{u}_w) \cdot \mathbf{n} < -l} f_{\alpha,l}^l}{\sum_{l=0}^{N-1} \sum_{(\mathbf{c}_{\alpha,l} - \mathbf{u}_w) \cdot \mathbf{n} > l} g_{\alpha}^{eq}(\mathbf{u}_w, T_w)} g_{\alpha}^{eq}(\mathbf{u}_w, T_w). \quad (12)$$

4. Numerical validation

We now examine our implementation scheme for Couette and lid-driven cavity flows. Four representative lattice models will be used for this purpose, namely D2Q17 [3], D2Q16 [27], D2Q37 [29] and D3Q121 [21,28], which are listed in Table 1 for convenience. The D2Q17 lattice is further illustrated in Fig. 1 and the corresponding ghost grid arrangement for a horizontal wall is shown in Fig. 2. Except for the corner points, the boundary condition is treated according to Eq. (12). The treatment for the corner points will be discussed late in the lid-driven cavity flow.

We test the implementation for the flows in the continuum ($Kn < 0.01$), continuum-slip ($0.01 \leq Kn < 0.1$) and early transition ($0.1 \leq Kn < 1$) regimes respectively. Simulation accuracy depends on the model accuracy which has already been extensively studied, see Refs. [2,3,10–15] and references therein. We will focus on the appropriateness of the present implementation of diffuse-reflection boundary condition rather than the accuracy of high-order models. For this purpose, it is sufficient to compare with the corresponding finite difference boundary condition implementation which has been proven to be appropriate for high-order models.

4.1. Isothermal and thermal Couette flows

The one-dimensional Couette flows are confined in two parallel planar plates located at $Y = 0$ and $Y = 1$ and moving oppositely with the same speed U_w , where all the quantities are presented in their non-dimensional form hereafter. We use the D2Q17 and D2Q16 models to investigate the isothermal flows and the D3Q121 model for the thermal flows.

The results are compared with the solutions of the Navier–Stokes–Fourier (NSF) equations at small Knudsen numbers and the linearized Boltzmann–BGK (L-BGK) equation for larger Knudsen numbers. For the NSF solutions, it is necessary to apply the velocity slip and temperature jump boundary conditions. The velocity profiles can be written as

$$U_{NSF} = \frac{(2y - 1)}{2Kn + 1} U_w, \quad (13)$$

and

$$T_{NSF} = \frac{Kn(8C_p T_w + 5u_w^2) + 8C_p T_w Kn^2 + 2C_p T_w - 4Pr U_w (Y - 1)Y}{2C_p (2Kn + 1)^2}, \quad (14)$$

Table 1

The lattices of four LB models where k is the number of discrete velocities with the same velocity magnitude, the subscript *FS* denotes a fully symmetric set of points. The details can be found in Refs. [3,21,27–29].

Quadrature	k	\mathbf{c}_α	\mathbf{w}_α	
D2Q16	4	$(\pm m, \pm m)$	$W_{\pm m}^2$	$m = 1, n = 4$
	4	$(\pm n, \pm n)$	$W_{\pm n}^2$	$W_{\pm m} = \frac{m^2 - 5n^2 + \sqrt{m^4 - 10n^2m^2 + n^4}}{12(m^2 - n^2)}$
	4	$(\pm m, \pm n)$	$W_{\pm m} W_{\pm n}$	$W_{\pm n} = \frac{5m^2 - n^2 - \sqrt{m^4 - 10n^2m^2 + n^4}}{12(m^2 - n^2)}$
	4	$(\pm n, \pm m)$	$W_{\pm m} W_{\pm n}$	$T_0 = (m^2 + n^2 + \sqrt{m^4 - 10n^2m^2 + n^4})/6$
D2Q17	1	$(0, 0)$	$\frac{575+193\sqrt{193}}{8100}$	
	4	$(r, 0)_{FS}$	$\frac{3355-91\sqrt{193}}{18000}$	
	4	$(\pm r, \pm r)$	$\frac{655+17\sqrt{193}}{27000}$	
	4	$(\pm 2r, \pm 2r)$	$\frac{685-49\sqrt{193}}{54000}$	
	4	$(3r, 0)_{FS}$	$\frac{1445-101\sqrt{193}}{162000}$	$r^2 = (125 + 5\sqrt{193})/72$
D2Q37	1	$(0, 0)$	0.23315066913235250228650	
	4	$(r, 0)_{FS}$	0.10730609154221900241246	
	4	$(\pm r, \pm r)$	0.05766785988879488203006	
	4	$(2r, 0)_{FS}$	0.01420821615845075026469	
	4	$(\pm 2r, \pm 2r)$	0.00101193759267357547541	
	4	$(3r, 0)_{FS}$	0.00024530102775771734547	
	8	$(r, 2r)_{FS}$	0.00535304900051377523273	
	8	$(r, 3r)_{FS}$	0.00028341425299419821740	$r = 1.19697977039307435897239$
D3Q121	1	$(0, 0, 0)$	$3.05916220294860 \times 10^{-2}$	
	6	$(r, 0, 0)_{FS}$	$9.85159510372633 \times 10^{-2}$	
	8	$(\pm r, \pm r, \pm r)_{FS}$	$2.75250053256381 \times 10^{-2}$	
	24	$(2r, r, 0)_{FS}$	$6.11102336683342 \times 10^{-3}$	
	12	$(2r, 2r, 0)_{FS}$	$4.28183593681084 \times 10^{-4}$	
	6	$(3r, 0, 0)_{FS}$	$3.24747527088073 \times 10^{-4}$	
	24	$(3r, 2r, 0)_{FS}$	$1.43186241154802 \times 10^{-5}$	
	8	$(\pm 2r, \pm 2r, \pm 2r)$	$1.81021751576374 \times 10^{-4}$	
	24	$(3r, r, r)_{FS}$	$1.06834002459391 \times 10^{-4}$	
	8	$(\pm 3r, \pm 3r, \pm 3r)$	$6.92875089638602 \times 10^{-7}$	$r = 1.19697977039307$

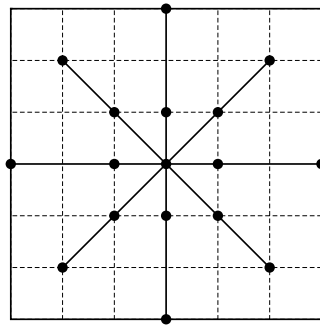


Fig. 1. Illustration of the D2Q17 lattice. Each discrete velocity is represented by the length and direction of the line connecting the origin of coordinate and the corresponding dotted point.

where the Knudsen number is defined as

$$Kn = \sqrt{\frac{\pi}{2}} \frac{\mu_0 \sqrt{RT_0}}{p_0 L}. \quad (15)$$

We evaluate our boundary condition implementation for the D2Q17 and D2Q16 models for the isothermal flows, and the results are presented in Figs. 3 and 4, where U_w is set to be 0.05. Both models are simulated with 100 computational grids in the direction of interest. The results show that the boundary condition of Eq. (12) works correctly for these flows. For $Kn \leq 0.05$, the velocity profiles are captured well by the D2Q17 model while some deviations from the L-BGK results are observed for larger Knudsen numbers, particularly at $Kn = 0.1$ (see Fig. 3). This is of no surprise as it is known that these deviations are due to the lattice structure [11]. Fig. 3 gives a further comparison to the finite difference (FD) implementation of Eq. (1), which confirms the appropriateness of the boundary condition implementation. Note, there are many finite difference schemes, for example, a scheme employed in Ref. [11], where the numerical simulation is validated by the analytical solution in Ref. [15]. Consistent with the observation in Ref. [11], the D2Q16 model can give much better predictions for the velocity profile even at $Kn = 0.5$ (see Fig. 4).

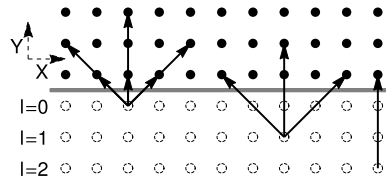


Fig. 2. Illustration of boundary treatment for the D2Q17 model, i.e. arrangement of the ghost grid and the corresponding outgoing discrete velocity. The solid circles denote the bulk grids while the dashed circles are the ghost grids. The outgoing distribution is obtained column by column according to Eq. (12).

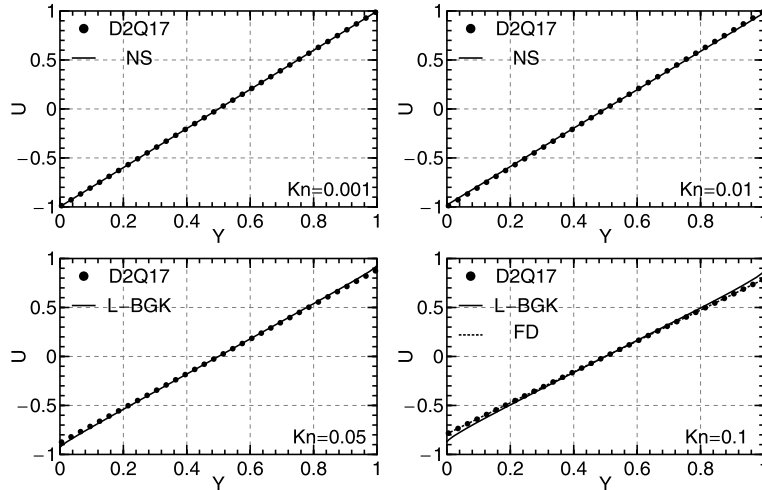


Fig. 3. Velocity profiles for the isothermal cases with the D2Q17 model. The velocity is further normalized by the wall velocity.

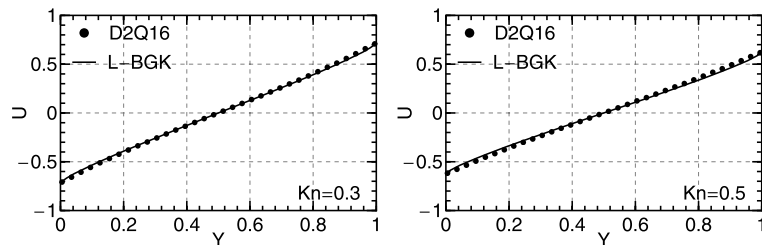


Fig. 4. Velocity profiles for the isothermal cases with the D2Q16 model. The velocity is further normalized by the wall velocity.

We also simulate the thermal Couette flows using the D3Q121 model. Again, we need to emphasize here is that we focus on our boundary condition implementation rather than evaluating the accuracy of any specific LB model. For these flows the relevant parameters are $C_p = 5/2$ and $Pr = 1$ while the wall temperatures are set to be 1 and their speed U_w is set to be 0.2. As relatively small Knudsen numbers are considered, the results are compared to the NSF solutions, see Fig. 5. The subtle temperature jumps are well captured at the wall boundary. These agreements again confirm the appropriateness of our boundary treatment. The velocity profiles show similar behavior to the isothermal cases, so they are not presented in Fig. 5. It is worth noting that the case for $Kn = 0.005$ is already in the continuum regime.

In Figs. 6–8, more results are presented for larger Knudsen numbers. They are compared with numerical solutions of the nonlinear BGK equation which are obtained in a manner similar to Ref. [33]. Similar to isothermal cases, the D3Q121 model already shows discrepancy for predictions of the temperature and the heat flux component Q_x in the stream-wise direction at $Kn = 0.1$, while the heat flux component Q_y in the span-wise direction still agrees with the results of the BGK equation. However, the errors become larger at $Kn = 0.5$. Nevertheless, the results agree with the corresponding finite difference implementation for the same D3Q121 model, which again confirms the correctness of boundary implementation. For the interest of LB model accuracy in terms of Knudsen number, particularly for thermal flows with adjustable Prandtl number, we refer to Ref. [2] where the accuracy has been examined extensively for various flows.

To evaluate the numerical accuracy, a convergence study is conducted for the thermal case of $Kn = 0.01$. The simulations are run for six different grid resolutions $N_G = 20, 50, 100, 200, 500, 1000$ in the direction of interest. The results of $N_G = 1000$ is then chosen as reference and the global relative errors of the velocity and temperature are defined as

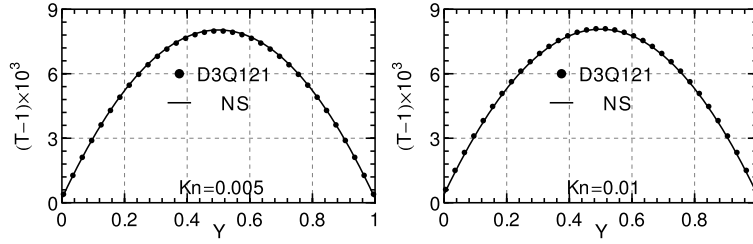


Fig. 5. Temperature profiles for the thermal cases with $U_w = 0.2$ and $Kn = 0.005, 0.01$.

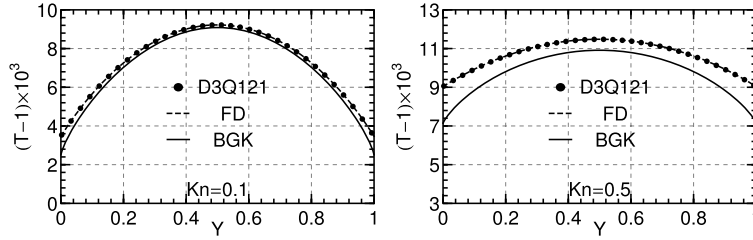


Fig. 6. Temperature profiles for the thermal cases with $U_w = 0.2$ and $Kn = 0.1, 0.5$.

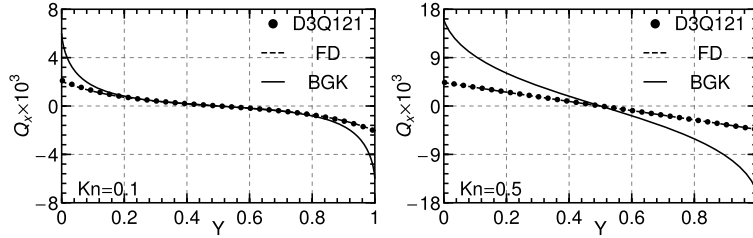


Fig. 7. Profiles of stream-wise heat flux component for the thermal cases with $U_w = 0.2$ and $Kn = 0.1, 0.5$.

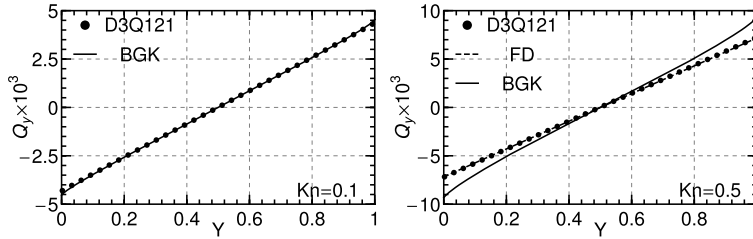


Fig. 8. Profiles of span-wise heat flux component for the thermal cases with $U_w = 0.2$ and $Kn = 0.1, 0.5$.

$$E_U = \sqrt{\frac{\sum_{j=1}^{N_G} [U_j(Y_j) - U_\Delta(Y_j)]^2}{\sum_{j=1}^{N_G} U_\Delta^2(Y_j)}}, \quad (16)$$

and

$$E_T = \sqrt{\frac{\sum_{j=1}^{N_G} [T_j(Y_j) - T_\Delta(Y_j)]^2}{\sum_{j=1}^{N_G} (T_\Delta(Y_j) - T_w)^2}}, \quad (17)$$

where U_Δ and T_Δ represent the results of $N_G = 1000$. Fig. 9 shows that the second order accuracy is achieved globally.

4.2. Lid-driven cavity flows

In the isothermal lid-driven cavity flow, the gas is contained in a two-dimensional geometry with rectangular cross section $L \times H$, where L is considered as the reference length which is used to define the Knudsen number (see Eq. (15)). In the non-dimensional system, the coordinates of four corners are $(0, 0)$, $(0, 1)$, $(0, A)$ and $(1, A)$ as shown in Fig. 10, where A is the ratio of H and L , i.e. H/L . The top wall is moving from left to right while the other three walls are stationary.

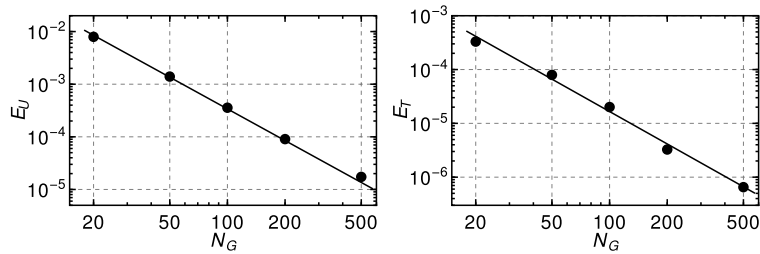


Fig. 9. Dependence of E_U and E_T on the grid number N_G .

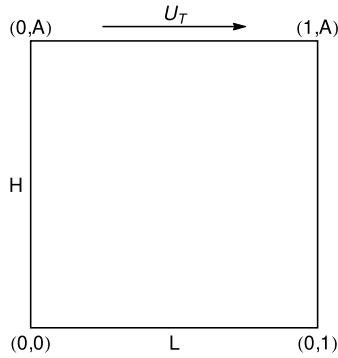


Fig. 10. Configuration of lid-driven cavity flows.

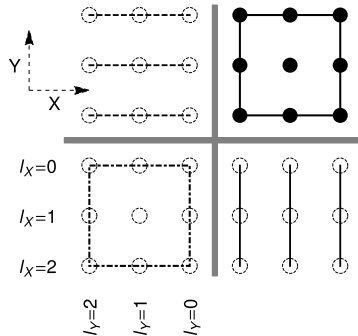


Fig. 11. Illustration of corner treatment for the D2Q17 model.

The nodes at four corners must be carefully treated. Unlike the normal vertical or horizontal wall (see the dashed and solid lines in Fig. 11), they cannot be treated either row by row or column by column. Otherwise non-physical gradient will be introduced. All corner nodes will be considered as a whole, see the ghost nodes within the dot-dashed square in Fig. 11, which represent the same physical wall corner. Their incoming distribution is from the bulk nodes within the solid square. Correspondingly, the formula of outgoing distribution becomes

$$f_{\alpha, l_X, l_Y}^0 = \frac{\sum_{l_Y=0}^{N-1} \sum_{l_X=0}^{N-1} \sum_{C_1} f_{\alpha, l}^I}{\sum_{l_Y=0}^{N-1} \sum_{l_X=0}^{N-1} \sum_{C_2} g_{\alpha}^{eq}(\mathbf{u}_w, T_w)} g_{\alpha}^{eq}(\mathbf{u}_w, T_w), \quad (18)$$

where C_1 represents the condition of $(\mathbf{c}'_{\alpha, l_X, l_Y} - \mathbf{u}_w) \cdot \mathbf{n}_X < -l_X \wedge (\mathbf{c}'_{\alpha, l_X, l_Y} - \mathbf{u}_w) \cdot \mathbf{n}_Y < -l_Y$ and C_2 of $(\mathbf{c}_{\alpha, l_X, l_Y} - \mathbf{u}_w) \cdot \mathbf{n}_X > l_X \wedge (\mathbf{c}_{\alpha, l_X, l_Y} - \mathbf{u}_w) \cdot \mathbf{n}_Y > l_Y$.

The difficulty is that the wall velocity U_W can be bi-valued for the corner points, particularly for the two top corners where strong discontinuities of velocity exist between the stationary and moving walls, which cause numerical problems. With increasing Knudsen number the problem may become even worse. To completely eliminate this, special treatment is needed as increasing the lattice points can only partly resolve the problem [30,31]. As our purpose is to test the implementation of boundary condition, we only consider the flows which do not need special treatment. The value of U_W for both two top corners can be set to be either U_T or zero, as no meaningful difference is observed for the cavity flow at $Kn = 0.05$.

The D2Q17 model is used and the Knudsen numbers are 0.008862 and 0.05, and $A = 1$. U_T is chosen to be 0.01 and the grid size is 0.01 in the non-dimensional system. Fig. 12 shows the profiles of the vertical and horizontal velocity components

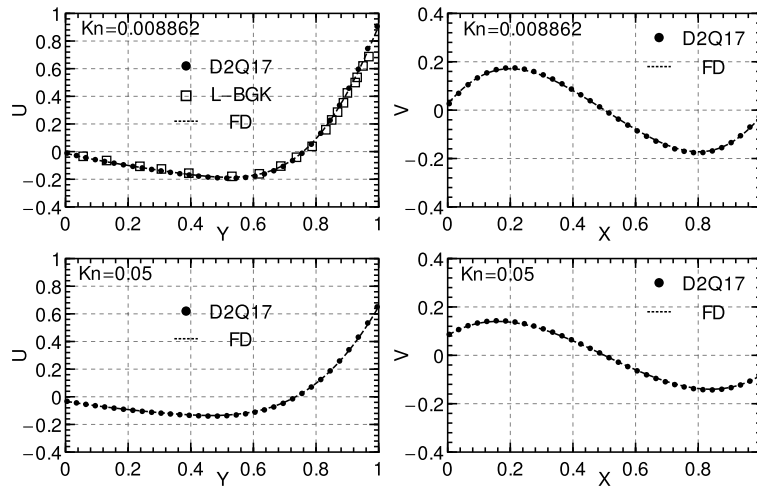


Fig. 12. Velocity profiles of the vertical V and horizontal U components along the horizontal and vertical centerlines of the cavity for various values of Kn and $A = 1$. The L-BGK result at $Kn = 0.008862$ is from Fig. 8 in Ref. [31]. The results are further normalized by $U_T = 0.01$.

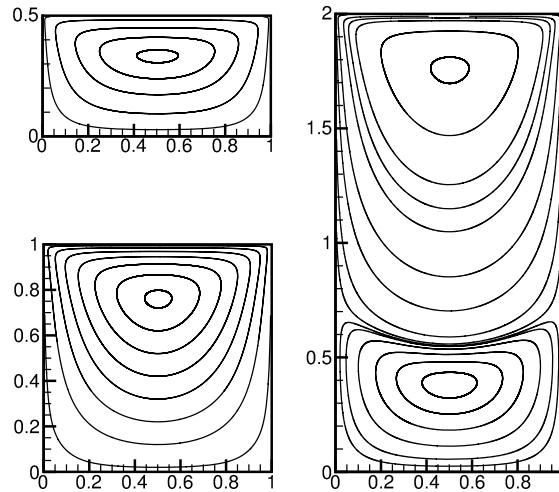


Fig. 13. Velocity streamlines predicted by the D2Q17 model for the lid-driven cavity flows at $Kn = 0.008862$ and $A = 0.5, 1$ and 2 .

along the centerlines of the cavity. For comparison, the results of the finite difference implementation for the D2Q17 model are presented, where the finite difference scheme used for this flow is a combination of the first-order and second-order upwind scheme without the time variable (cf. Ref. [32] and references therein). In particular, a set of data from Fig. 5 of Ref. [31] is presented for the horizontal velocity component at $Kn = 0.008862$. The agreements confirm the validity of the present boundary implementation.

More geometry configurations are simulated for $Kn = 0.008862$ with $A = 0.5$ and 2 . Their velocity streamlines are plotted in Fig. 13. Qualitative agreement can be found with those given in Fig. 5 of Ref. [31]. For example, there are two vortices for the case of $A = 2$.

It is also interesting to investigate the results for smaller Knudsen numbers. Figs. 14 and 15 show the results for $Kn = 0.0001$, $U_T = 0.05$, $A = 1$. The Reynolds number is 500 as $Re = Kn/Ma$ where Ma is defined as $Ma = U_T$ in the non-dimensional system. For this case, the D2Q17 model is employed again and 320×320 grids are used. The results confirm the potential of applying the diffuse-reflection boundary condition for flows in the continuum regime ($Kn < 0.01$).

In order to further test the boundary implementation, a thermal cavity case is also considered using the D2Q37 model. Similar to the isothermal cases, the relevant parameters are chosen as $A = 1$, $Kn = 0.01$ and $U_T = 0.05$. The difference is that the wall temperatures are not uniform now. Instead, the left wall temperature is set to be 1 while the right wall temperature is 1.05 . Correspondingly, the temperatures at both top and bottom walls are distributed linearly. The results are shown in Figs. 16–18. The agreements with the corresponding finite difference results further validate the present implementation.

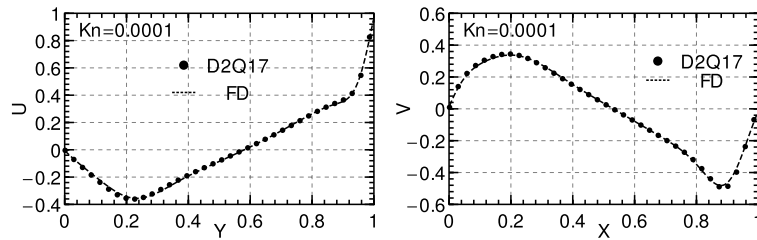


Fig. 14. Velocity profiles of vertical (V) and horizontal (U) components along the horizontal and vertical centerlines of the cavity for $Kn = 0.0001$. The results are further normalized by $U_T = 0.05$.

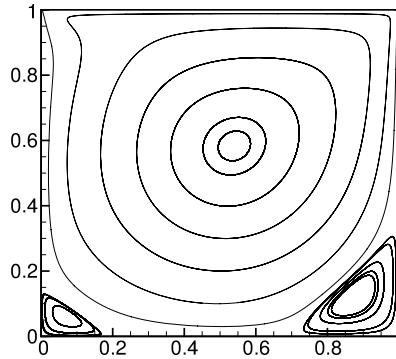


Fig. 15. Velocity streamlines predicted by the D2Q17 model for the lid-driven cavity flows at $Kn = 0.0001$, $A = 1$, $U_T = 0.05$ and $Re = 500$.

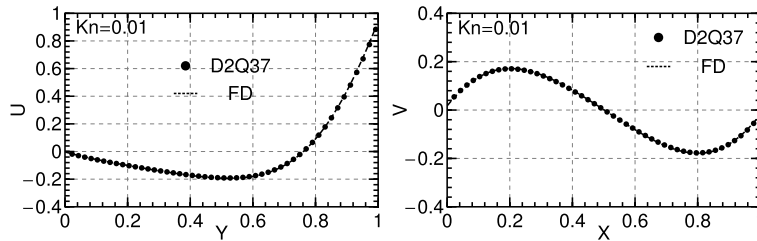


Fig. 16. Velocity profiles of the vertical V and horizontal U components along the horizontal and vertical centerlines of the cavity for the thermal case.

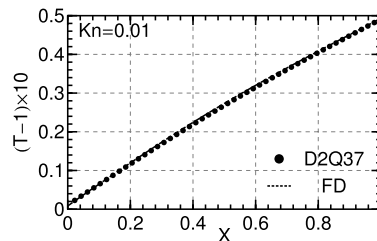


Fig. 17. Temperature profiles along the horizontal centerlines of the cavity for the thermal case.

5. Concluding remarks

To conclude, we have studied the implementation of the diffuse reflection boundary condition for high-order LB models with emphasis on retaining the “streaming–collision” mechanism. Our new implementation is tested for the isothermal and thermal Couette flows and the lid-driven cavity flows using lattice models. By comparing with the corresponding finite difference implementation and the results of L-BGK and nonlinear BGK model, it is found that the velocity slip and temperature jump at the walls are correctly reproduced within the capability of the chosen lattice models. For the thermal Couette flow it is found that the present scheme can achieve second-order accuracy globally at $Kn = 0.01$. Not only is the diffuse-reflection boundary condition used to capture rarefaction effects in this work, it is also tested for hydrodynamic flows where the Knudsen is very small and the Reynolds number is significant. In the future, we will investigate the present scheme for flows in more complex geometries.

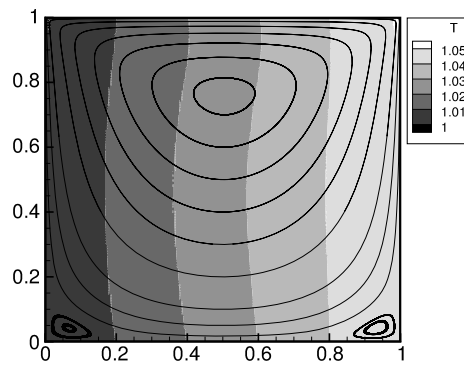


Fig. 18. Velocity streamlines and temperature contour predicted by the D2Q37 model.

Acknowledgements

The authors would like to thank Dr. Xiaowen Shan for many informative discussions. The research leading to these results has received funding from the Engineering and Physical Sciences Research Council U.K. under Grants No. EP/F028865/1 and EP/I036117/1.

References

- [1] X. Nie, X. Shan, H. Chen, Lattice-Boltzmann/finite-difference hybrid simulation of transonic flow, in: 47th AIAA Aerospace Sciences Meeting, January 2009, AIAA 2009-139, http://pdf.aiaa.org/preview/CDReadyMASM09_1811/PV2009_139.pdf.
- [2] J. Meng, Y. Zhang, N.G. Hadjiconstantinou, G.A. Radtke, X. Shan, Lattice ellipsoidal statistical BGK model for thermal non-equilibrium flows, *J. Fluid Mech.* 718 (2013) 347–370, http://journals.cambridge.org/article_S0022112012006167.
- [3] X.W. Shan, X.F. Yuan, H.D. Chen, Kinetic theory representation of hydrodynamics: A way beyond the Navier–Stokes equation, *J. Fluid Mech.* 550 (2006) 413–441.
- [4] P.C. Philippi, L.A. Hegele Jr., L.O.E. Dos Santos, R. Surmas, From the continuous to the lattice Boltzmann equation: The discretization problem and thermal models, *Phys. Rev. E* 73 (2006) 056702.
- [5] S.S. Chikatamarla, I.V. Karlin, Entropy and Galilean invariance of lattice Boltzmann theories, *Phys. Rev. Lett.* 97 (2006) 190601.
- [6] D. Lycett-Brown, I. Karlin, K.H. Luo, Droplet collision simulation by a multi-speed lattice Boltzmann method, *Commun. Comput. Phys.* 9 (5) (2011) 1219–1234, <http://www.global-sci.com/issue/abstract/readabs.php?vol=9&page=1219&issue=5&ppage=1234&year=2011>.
- [7] P.C. Philippi, K.K. Mattila, D.N. Siebert, L.O.E. dos Santos, L.A. Hegele Jr., R. Surmas, Lattice-Boltzmann equations for describing segregation in non-ideal mixtures, *J. Fluid Mech.* 713 (2012) 564–587.
- [8] P.C. Philippi, L.O.E. dos Santos, L.A. Hegele Jr., C.E.P. Ortiz, D.N. Siebert, R. Surmas, Thermodynamic consistency in deriving lattice Boltzmann models for describing segregation in non-ideal mixtures, *Philos. Trans. R. Soc. Lond. A* 369 (2011) 2292–2300.
- [9] A. Scagliarini, L. Biferale, M. Sbragaglia, K. Sugiyama, F. Toschi, Lattice Boltzmann methods for thermal flows: Continuum limit and applications to compressible Rayleigh–Taylor systems, *Phys. Fluids* 22 (2010) 055101.
- [10] J. Meng, Y. Zhang, Accuracy analysis of high-order lattice Boltzmann models for rarefied gas flows, *J. Comput. Phys.* 230 (3) (2011) 835–849, <http://linkinghub.elsevier.com/retrieve/pii/S0021999110005796>.
- [11] J. Meng, Y. Zhang, Gauss–Hermite quadratures and accuracy of lattice Boltzmann models for nonequilibrium gas flows, *Phys. Rev. E* 83 (3) (2011) 036704, <http://pre.aps.org/abstract/PRE/v83/i3/e036704>.
- [12] F. Verhaeghe, L.-S. Luo, B. Blanpain, Lattice Boltzmann modeling of microchannel flow in slip flow regime, *J. Comput. Phys.* 228 (1) (2009) 147–157.
- [13] M. Watari, Velocity slip and temperature jump simulations by the three-dimensional thermal finite-difference lattice Boltzmann method, *Phys. Rev. E* 79 (6) (2009) 66706.
- [14] S.H. Kim, H. Pitsch, I.D. Boyd, Accuracy of higher-order lattice Boltzmann methods for microscale flows with finite Knudsen numbers, *J. Comput. Phys.* 227 (19) (2008) 8655–8671.
- [15] S. Ansumali, I.V. Karlin, S. Arcidiacono, A. Abbas, N.I. Prasianakis, Hydrodynamics beyond Navier–Stokes: Exact solution to the lattice Boltzmann hierarchy, *Phys. Rev. Lett.* 98 (12) (2007) 124502.
- [16] P. Taheri, M. Torrilhon, H. Struchtrup, Couette and Poiseuille microflows: Analytical solutions for regularized 13-moment equations, *Phys. Fluids* 21 (1) (2009) 17102.
- [17] V. Sofonea, Implementation of diffuse reflection boundary conditions in a thermal lattice Boltzmann model with flux limiters, *J. Comput. Phys.* 228 (17) (2009) 6107–6118.
- [18] X.W. Shan, X.Y. He, Discretization of the velocity space in the solution of the Boltzmann equation, *Phys. Rev. Lett.* 80 (1) (1998) 65–68.
- [19] X. He, Q. Zou, L.-S. Luo, M. Dembo, Analytic solutions of simple flows and analysis of nonslip boundary conditions for the lattice Boltzmann BGK model, *J. Stat. Phys.* 87 (1) (1997) 115–136.
- [20] S.S. Chikatamarla, I.V. Karlin, Lattices for the lattice Boltzmann method, *Phys. Rev. E* 79 (4) (2009) 46701.
- [21] X. Shan, General solution of lattices for Cartesian lattice Bhatnagar–Gross–Krook models, *Phys. Rev. E* 81 (3) (2010) 36702.
- [22] X. He, S. Chen, G.D. Doolen, A novel thermal model for the lattice Boltzmann method in incompressible limit, *J. Comput. Phys.* 146 (1) (1998) 282–300.
- [23] C. Cercignani, *Rarefied Gas Dynamics from Basic Concepts to Actual Calculations*, Cambridge University Press, 2000.
- [24] S. Ansumali, I.V. Karlin, Kinetic boundary conditions in the lattice Boltzmann method, *Phys. Rev. E* 66 (2) (2002) 26311.
- [25] S.Y. Chen, G.D. Doolen, Lattice Boltzmann method for fluid flows, *Annu. Rev. Fluid Mech.* 30 (1998) 329–364.
- [26] R. Gatignol, Kinetic theory boundary conditions for discrete velocity gases, *Phys. Fluids* 20 (12) (1977) 2022–2030.
- [27] S.S. Chikatamarla, I.V. Karlin, Entropy and Galilean invariance of lattice Boltzmann theories, *Phys. Rev. Lett.* 97 (19) (2006) 190601.
- [28] X. Nie, X. Shan, H. Chen, Thermal lattice Boltzmann model for gases with internal degrees of freedom, *Phys. Rev. E* 77 (3) (2008) 1–4, <http://link.aps.org/doi/10.1103/PhysRevE.77.035701>.
- [29] X.W. Shan, H.D. Chen, A general multiple-relaxation Boltzmann collision model, *Int. J. Mod. Phys. C* 18 (2007) 635–643.

- [30] K. Aoki, C. Bardos, C. Dogbe, F. Golse, A note on the propagation of boundary induced discontinuities in kinetic theory, *Math. Models Methods Appl. Sci.* 11 (9) (2001) 1581–1595, <http://www.worldscientific.com/doi/abs/10.1142/S0218202501001483>.
- [31] S. Naris, D. Valougeorgis, The driven cavity flow over the whole range of the Knudsen number, *Phys. Fluids* 17 (9) (2005) 97106.
- [32] K. Aoki, S. Takata, T. Nakanishi, Poiseuille-type flow of a rarefied gas between two parallel plates driven by a uniform external force, *Phys. Rev. E* 65 (2) (2002) 26315.
- [33] J.P. Meng, L. Wu, J.M. Reese, Y.H. Zhang, Assessment of the ellipsoidal-statistical Bhatnagar–Gross–Krook model for force-driven Poiseuille flows, *J. Comput. Phys.* 251 (2013) 383–395.